LAWRENCE
LIVERMORE
NATIONAL
LABORATORY

UCRL-JRNL-206107

Ceramic Coatings for Corrosion Resistant Nuclear Waste Container Evaluated in Simulated Ground Water at 90°C

Jeffery J. Haslam, Joseph C. Farmer, Robert W. Hopper, Keith R. Wilfinger

August 17, 2004

Metallurgical and Materials Transactions A

Disclaimer

Ceramic Coatings for Corrosion Resistant Nuclear Waste Container Evaluated in Simulated Ground Water at 90°C

Dr. Jeffery J. Haslam, Dr. Joseph C. Farmer, Dr. Robert W. Hopper, and Dr. Keith R. Wilfinger
Lawrence Livermore National Laboratory
7000 East Avenue, L-353
Livermore, California 94550
Email: haslam2@llnl.gov

This work was performed under the auspices of the U.S. Department of Energy by University of California, Lawrence Livermore National Laboratory under Contract W-7405-Eng-48.

Abstract

Ceramic materials provide an innovative opportunity for corrosion resistant coatings for nuclear waste containers. Their suitability can be derived from the fully oxidized state for selected metal oxides. Ceramic coatings applied to plain carbon steel substrates by several thermal spray techniques have been exposed to 90°C simulated ground water (at ten times typical concentration) for nearly 6 years. Thermal spray processes examined in this work included plasma spray, High Velocity Oxy Fuel (HVOF), and Detonation Gun. Some thermal spray coatings have demonstrated superior corrosion protection for the plain carbon steel substrate. In particular the HVOF and Detonation Gun thermal spray processes produced coatings with low connected porosity, which limited the growth rate of corrosion products. It was also demonstrated that these coatings resisted spallation of the coating even when an intentional flaw (which allowed for corrosion of the carbon steel substrate underneath the ceramic coating) was placed in the coating. An approach for a theoretical basis for prediction of the corrosion protection provided by ceramic coatings is also presented. The theoretical development includes the effect of the morphology and amount of the porosity within the thermal spray coating and provides a prediction of the exposure time needed to produce a crack in the ceramic coating.

UCRL-JRNL-206107

Introduction

The United States currently intends to provide a reliable storage of spent fuel rods from nuclear reactors and high level nuclear waste in a below ground repository for a period of time exceeding 10,000 years and possibly longer. While there are many facets of providing reliable protection of the waste material to prevent adverse effects on the environment, a particular challenge is corrosion of the waste package by aqueous environments in the proposed repository [1]. Under extreme conditions of high temperature oxidizing or acid environments it may be difficult to find metals that will protect against corrosion. Inorganic oxide materials (ceramics) may be the only materials that can provide sufficiently low dissolution rates of container materials under these conditions. Additionally, in some scenarios use of ceramic coatings on metallic substrates would provide significant cost savings to the waste package design and mitigate aggressive crevice corrosion conditions. In particular covalent oxide compounds in their highest normal oxidation states are unlikely to participate directly in electrochemical or galvanic corrosion mechanisms. It is helpful to consider that an inorganic oxide film is a relatively thick and fully oxidized version of the passivating films that generally are responsible for corrosion-resistance in many metals. It is expected that with the constituent elements in their fully oxidized state dissolution mechanisms are the only likely material loss process for covalent metal oxide compounds.

While there are several ways to produce ceramic coatings, for this application corrosion resistant coatings with a solid impervious coating of about 400 μm (0.015 inch) or greater is desirable. Thermal spray processes potentially can provide an impervious coating of this thickness in an industrially amenable process. Plasma thermal spray technology uses a plasma to produce heating and acceleration of coating particles in the spray gun. Powder is fed into the plasma and accelerated by the expanding gas used to form the plasma. The heated molten particles hit the substrate and deform and cool to form a densified film. Other thermal spray technologies use a similar approach of heating and accelerating the particles to high velocity. High Velocity Oxy-Fuel (HVOF) and Detonation Gun spray processes generally can produce higher velocities to produce greater deformation of the particles when the particles hit the substrate. The porosity that remains in most thermal spray coatings is associated with the interfaces between the particles. In particular HVOF and Detonation Gun [2] coatings have shown the possibility of water impervious inorganic coatings. It is also anticipated that these coating approaches may also be useful for other applications requiring corrosion protection. Since it is not easy to obtain experimental evidence for corrosion performance of most materials for thousands years, predictive calculations based on theory are one means of estimating the possible performance of a corrosion barrier over long periods of time. Some fundamental equations are developed to predict corrosion performance of the inorganic coatings using properties of the coating microstructure. It is difficult to have confidence in extrapolating data to time frames that exceed the experiments by many orders of magnitude. However, to increase confidence in the predictions rather conservative assumptions are made to help estimate likely minimum performance over long time periods.

Coating Techniques

Plasma spray utilizes the discharge of electricity through a plasma gas to create a very high temperature zone within the spray gun. The powder is fed into this plasma and simultaneously heated and accelerated towards a substrate where the powder particles hit the substrate, which cools the molten particles rapidly to form a solid coating. The high temperature in the plasma under proper conditions will usually melt ceramic particles. Propelling the particles towards the substrate at high velocity is critical in helping to deform the molten particles to form a coating that has a much higher density than random packing of the particles without the deformation. Both heating and velocity of the particles are important to producing strong dense coatings. Plasma spray does not always produce the highest particle velocity (most generally 125 to 325 m/s) although it is often capable of very high temperatures. The substrate for the coating often functions as an effective heat sink to rapidly solidify the ceramic particles.

High Velocity Oxy-Fuel (HVOF) thermal spray is a slightly different type of coating process. In this case the thermal spray gun functions as a supersonic combustion nozzle. Fuel and oxidizing gases are supplied to the combustion chamber along with the powder (usually the powder is delivered with a carrier gas) where the combustion produces supersonic flow through a nozzle within the gun. The powder is accelerated to relatively high velocities while being heated by the combustion process. Generally, much higher particle velocities (up to 550 m/s and sometimes higher) can be obtained with HVOF thermal spray. Under the right operating conditions this leads to relatively higher density coatings. This is primarily attributed to the higher particle velocities, which produce greater deformation to aid in causing the particles to conform to both the substrate and coating particles already applied to the substrate.

Detonation Gun thermal spray uses a similar gun design to HVOF except that a supersonic nozzle is not present. The combustion process is pulsed by a spark ignition of the fuel and oxidizer. Even higher particle velocities (up to 800 m/s) are obtained using the Detonation Gun. The Detonation Gun designs have often included valves to cycle the flow of fuel and oxidizer to the combustion chamber; however, more recent designs have resulted in a valve-less Detonation Gun. More extensive descriptions of these thermal spray techniques are available in the literature [3].

Theoretical Background for Predicting Lifetime of Coating

Theoretical models of idealized inorganic coatings have been developed for various environmental conditions during anticipated repository conditions [4]. During the periods of dry oxidation ($T \geq 100°C$) and humid-air corrosion ($T \leq 100°C$ and $RH < 80\%$), it is assumed that the growth rate of oxide on the surface is diminished in proportion to the amount of surface covered by solid ceramic. During the period of aqueous phase corrosion ($T \leq 100°C$ and $RH \geq 80\%$), it is assumed that the overall mass transfer resistance governing the corrosion rate can be due to the combined resistances of ceramic coating and interfacial corrosion products. Modeling of only the aqueous

corrosion regime is presented here. A simple porosity model (cylinder and sphere chain) is considered to estimate the mass transfer resistance of the ceramic coating. It is evident that resistance to O_2 transport is encountered if pores are filled with liquid water. Spallation (rupture) of the ceramic coating is assumed to occur if the stress introduced by the expanding corrosion products at the ceramic-metal interface exceeds the fracture stress of the ceramic.

Corrosion Reactions

The corrosion products formed on carbon steel in vapor-phase environments have included goethite (α-FeOOH) and magnetite (Fe_3O_4). In aqueous phase environments that contain chloride salts, corrosion products may also include akaganeite (β-FeOOH). These products have been identified by Raman spectroscopy, and confirmed by X-ray diffraction [4]. In terms of aqueous-phase corrosion process two likely limiting processes for steady-state corrosion exist: 1) transport of oxygen to the interface, 2) transport of corrosion products away from the interface. The corrosion of steel at the metal/ceramic interface requires the simultaneous oxidation of iron and reduction of oxygen. In the case of aqueous phase corrosion, it has been shown that dissolved oxygen is required as a cathodic reactant to promote corrosion. For our purposes here we have assumed that oxygen transport may be the rate limiting corrosion transport step in these coatings. Since the formation of magnetite at the ceramic-metal interface would be most detrimental to the coating (based on volume change), we assume that all of the corrosion product is in the form of Fe_3O_4. Although, the actual corrosion product may be more complicated, it is taken as a conservative estimate to help provide an upper bound to the stress produced by growth of corrosion product. Further, it is also assumed that the oxygen must diffuse all the way through the corrosion product to the metal substrate even though in actual corrosion conditions this process may be different. Oxyhydroxides such as FeOOH would probably be present as polymeric gels at the interface; however, due to the likely compliance of the gel, FeOOH was not considered. The chemical reaction for the theoretical development reported here is: $3Fe + 2O_2 \longrightarrow Fe_3O_4$, which is composed of the half-reactions:

$$\begin{aligned} Fe &\longrightarrow Fe^{2+,3+} \\ 1/2O_2 &\longrightarrow O^{2-}. \end{aligned} \qquad (1)$$

Aqueous Phase Corrosion

Pores are completely filled with moisture in the aqueous phase corrosion analysis. Typical aqueous phase corrosion rates apply at the ceramic-metal interface when dripping water exists and the relative humidity (RH) is greater than 80%. It is well known that aqueous phase corrosion of carbon steel relies heavily on the cathodic reduction of oxygen for depolarization of the anodic reaction [5]. Measurements show corrosion rates increase linearly with the concentration of dissolved oxygen. The rate in completely de-aerated solution (zero concentration of dissolved oxygen) appears to be essentially zero (infinitesimally small). Therefore, the following oxygen-dependent penetration rate is assumed:

$$\frac{1}{3}\frac{\rho}{w}\frac{dp}{dt} = \frac{1}{2}k_O C \qquad (2)$$

where C (in this case) is the concentration of dissolved oxygen in water contacting the carbon steel. In most cases, C is equivalent to the saturation concentration, C_{sat}. From the published data of Uhlig and Revie [5], the extrapolated penetration rate of carbon steel after 48 hours exposure at 25°C to a solution containing 165 ppm $CaCl_2$ and 6 ml/liter dissolved O_2 is approximately 93.46 mg/dm^2/day (0.43345 mm/year). The apparent rate constant, k_0, can be calculated from the slope of this plotted data, which is 15.576 mg/dm^2/day per ml/liter.

The following equation provides the concentration of dissolved oxygen in the water contacting the carbon steel as a function of temperature and salt concentration [6].

$$\ln(C_{sat}) = A_1 + A_2\left(\frac{100}{T}\right) + A_3\ln\left(\frac{T}{100}\right) + A_4\left(\frac{T}{100}\right) + S\left[B_1 + B_2\left(\frac{T}{100}\right) + B_3\left(\frac{T}{100}\right)^2\right] \qquad (3)$$

In this equation, C_{sat} is the saturation concentration of dissolved oxygen in water (ml O_2 per liter H_2O), T is the absolute temperature (K), and S is the total concentration of dissolved salt (parts per thousand). The coefficients A_i and B_i are defined in Table I below.

Table I. Coefficients for the Calculation of Dissolved Oxygen in Salt-Containing Water

Coefficient	i = 1	i = 2	i = 3	I = 4
A_i	-173.4292	249.6330	143.3483	-21.033096
B_i	-0.033096	0.014259	-0.0017000	

Conversion of this quantity (ml O_2 per liter of H_2O) to more conventional units is done as follows:

$$C_{sat}(mol/cm^3) = B\frac{P}{RT}C_{sat}(ml/liter) \qquad (4)$$

where P is atmospheric pressure (atm), T is the absolute temperature (K), R is the universal gas constant (82.056 atm cm^3 mol^{-1} K^{-1}), and B is a conversion factor (0.001 liters per cm^3).

Diffusive Flux through the Porous Ceramic Coating

Development of an appropriate model begins with consideration of the flux of oxygen, J, through multiple diffusion barriers, represented by subscripts I and 0 (see Figure 1).

$$J = k_I(a - a_i) = k_O(a_i - a_s) = K(a - a_s) \tag{5}$$

The parameters k_I and k_0 are the individual mass transfer coefficients for barriers *I* and *0*, respectively, k is the overall mass transfer coefficient for both barriers, a is the activity of the transported reactive species at the outer surface of barrier *I*, a_i is the activity at the interface separating barriers *I* and *0*, and a_s is the activity at the interface separating barrier *0* and the metal substrate. The barrier *I* represents the ceramic coating, the barrier *0* represents the accumulated interfacial corrosion product Fe_3O_4, the metal substrate is carbon steel, and the transported reactive species is dissolved oxygen in pore water (aqueous phase corrosion). Furthermore, it is also assumed that the chemical activity, a, can be approximated by concentration, C.

Physical Definition of Overall Mass Transfer Coefficient (Resistance)

The overall mass transfer coefficient (mass transfer resistance) can be expressed in terms of the individual mass transfer coefficients as described by Sherwood, Pigford and Wilke [7].

$$\frac{1}{K} = \frac{1}{k_0} + \frac{1}{k_I} \tag{6}$$

The individual mass transfer coefficients are given physical definition by introducing a simple porosity model. For example, in the case of the ceramic coating, pores are first treated as long, straight cylinders of length δ. The flux, J, of corroding species through such a pore is then approximated by:

$$J_{pore} = \frac{D_I}{\delta}(C - C_i) \tag{7}$$

The average flux of oxygen per unit area of waste package is then:

$$J = \frac{\theta_I D_I}{\delta}(C - C_i) \tag{8}$$

where D_I is the bulk diffusivity of the corroding species in the pore and θ_I is the fraction of the metal exposed to the aqueous phase at the ceramic-metal interface. This can be interpreted as porosity. Values of 0.02-0.03 have been achieved with HVOF ceramic coatings having a thickness of approximately 1.5 mm. Since the corrosion product is also likely to be porous, the interfacial corrosion product can be modeled in a similar fashion:

$$J = \frac{\theta_O D_O}{x}(C_i - C_s) \tag{9}$$

where x is the thickness of the accumulated corrosion product, D_0 is the effective diffusivity of the corroding species through the accumulated corrosion product and θ_0 is

the effective porosity of the accumulated corrosion product. At the point when the reaction of corroding species with the metal substrate becomes entirely mass-transport limited, the concentration C_s drops to zero. Assuming straight cylindrical pores, the physical definition of the overall mass transfer coefficient is then:

$$\frac{1}{K} = \frac{1}{k_0} + \frac{1}{k_I} = \frac{x}{\theta_O D_O} + \frac{\delta}{\theta_I D_I} \tag{10}$$

In reality, the pores in the ceramic coating are not as simple as portrayed in the above straight hollow cylinder representation. The pores in ceramic coatings can better be represented by an array of chains, each link being composed of a hollow sphere and a relatively narrow hollow cylinder, as illustrated in Figure 2. Various models of this sort have been considered, the simplest of which has become known as the cylinder-sphere chain (CSC) porosity model, consists of straight chains with identical links, located randomly and oriented normal to the surface. The calculations that follow are based on it. A heuristically more satisfying model, in which the chains are interconnected to form a three-dimensional network, gives for all practical purposes equivalent results. A discussion of the improved models — physical rationales, analysis descriptions, extensions and limitations — is given in Appendix A.

$$k_{I,corrected} = f(\varepsilon, \lambda) \times k_I \tag{11}$$

where f($\varepsilon\lambda$) is defined as:

$$f(\varepsilon, \lambda) = \frac{3}{2} \frac{(1+\lambda)^2}{\lambda} \varepsilon^2 \tag{12}$$

Thus, the overall mass transfer coefficient is defined as:

$$\frac{1}{K} = \frac{x}{\theta_0 D_0} + \frac{\delta}{f(\varepsilon, \lambda)\theta_I D_I} \tag{13}$$

Here the dimensionless parameters ε and λ represent the geometry of the sphere-cylinder chain as illustrated in Figure 2:

$$\varepsilon = \frac{diameter\ of\ cylinder\ \ in\ chain}{diameter\ of\ \ sphere\ \ in\ chain} \tag{14}$$

$$\lambda = \frac{length\ of\ \ cylinder\ \ in\ chain}{diameter\ of\ \ sphere\ \ in\ chain} \tag{15}$$

Reasonable estimates for ε and λ, based on actual microstructures, are as follows:

$$0.01 \le \varepsilon \le 0.10 \tag{16}$$

$$2 \le \lambda \le 10 \tag{17}$$

Typical values of $f(\varepsilon,\lambda)$ are illustrated below:

$$f(0.03,10) = 0.016$$
$$f(0.05,10) = 0.045$$

Parabolic Isothermal Growth of Interfacial Oxide with O_2 Reduction Alone

Formation of one (1) mole of Fe_3O_4 requires the transport of two (2) moles of molecular oxygen and the consumption of three (3) moles of iron. Stated in a slightly different way, the molar production rate of Fe_3O_4 is one-third (1/3) that of the molar consumption rate of iron and one-half (1/2) the molar consumption rate of molecular oxygen. Therefore, a relationship is established between the flux of corroding species through the protective ceramic coating, the penetration rate of the carbon steel (*dp/dt*), and the growth rate of the interfacial oxide (*dx/dt*):

$$\frac{\rho_O}{w_O}\frac{dx}{dt} = \frac{1}{3}\frac{\rho}{w}\frac{dp}{dt} = \frac{1}{2}J = \frac{1}{2}KC \tag{18}$$

After substitution of the expression for the overall mass transfer coefficient (equation 10), this equation is rearranged to yield:

$$\frac{dx}{dt} = \frac{w_0}{\rho_0}\left\{\left[\frac{x}{\theta_0 D_0} + \frac{\delta}{f(\varepsilon,\lambda)\theta_I D_I}\right]^{-1}\frac{C}{2}\right\} \tag{19}$$

This expression can be rearranged and then integrated, assuming isothermal conditions, to determine the dependence of the interfacial oxide thickness on time.

The solution of the resulting simple quadratic equation yields the following relationship between oxide thickness, time and ceramic coating properties (see appendix B):

$$x = \left[\left\{\frac{\delta}{f(\varepsilon,\lambda)}\frac{\theta_0 D_0}{\theta_I D_I}\right\}^2 + (\theta_0 D_0)\frac{w_0}{\rho_0}Ct\right]^{1/2} - \left\{\frac{\delta}{f(\varepsilon,\lambda)}\frac{\theta_0 D_0}{\theta_I D_I}\right\} \tag{20}$$

The thickness of the interfacial oxide increases with time. As the oxide becomes thicker, the growth rate decreases (Wagner's law). The relationship between oxide thickness and wall penetration is:

$$x = \frac{1}{3}\left(\frac{\rho}{\rho_0}\frac{w_0}{w}\right)p \tag{21}$$

However, as a conservative approximation the oxide can be assumed to still grow at a linear rate with time, which produces a thicker oxide and consequently greater stress in less time.

First Failure Criterion: Membrane Stress in Expanded Cylinder

Two alternative stress models are presented to account for spallation of the ceramic coating. In the first case, the ceramic coating is treated as a cylindrical membrane having infinitesimal thickness, as shown in Figure 3. A fracture toughness criterion would likely be more appropriate but for the results presented here a simple failure stress will be considered to include the effects of flaw population size in the coatings. The rate of expansion of the inner radius of the ceramic barrier coating is estimated from the interfacial displacement, which accounts for the conversion of Fe to Fe_3O_4 (expansion), as well as the simultaneous loss of carbon steel (contraction).

$$\frac{dR}{dt} = \frac{d(x-p)}{dt} \tag{22}$$

The difference between the oxide thickness and the wall penetration $(x-p)$ is defined as the interfacial displacement. The strain in the coating, around the circumference of the container, is proportional to the change in inner radius

$$\frac{de}{dt} = \frac{1}{2\pi R}2\pi\frac{dR}{dt} \tag{23}$$

which can be written more simply as:

$$\frac{de}{dt} = \frac{1}{R}\frac{dR}{dt} \tag{24}$$

The uniaxial stress and strain are related by the elastic modulus, E:

$$\sigma = E \times e \tag{25}$$

For example, the fracture strain of a porous ceramic exposed to water can be estimated from the elastic modulus and the fracture stress as follows:

$$e^* = \frac{\sigma^*}{E} = \frac{16.7\,MPa}{356{,}000\,MPa} = 4.691\times10^{-5} = 0.0047\% \tag{26}$$

The time required for the strain to reach the fracture strain, τ^*, determines the time to fracture. This is the time required for formation of the first crack in the ceramic coating, but does not necessarily imply complete failure of the coating.

$$\tau^* = \frac{e^*}{\int_0^t \frac{de}{dt} dt} \tag{27}$$

Second Failure Criterion: Blistering

In this failure process it is assumed that spallation occurs at a blister, such as the one illustrated in Figure 4. To account for the formation of blisters in the ceramic coating, Roark's formulas can be used [8]. The deflection of the center of the circular plate from the relaxed position is y_c, defined as follows:

$$y_c = -\frac{qa^4}{64D} \tag{28}$$

where q is the uniform load (pressure) exerted on the internal surface of the deflected circular plate (blister), a is the radius of the circular plate (blister), and D is the plate constant. The subscript, c, is used to indicate the outermost surface where the stress is highest. Since the deflection is known (interfacial displacement), the uniform load can be calculated.

$$q = -\frac{64D}{a^4} y_c \tag{29}$$

The plate constant is given by:

$$D = -\frac{Et^3}{12(1-\upsilon^2)} \tag{30}$$

where E is the elastic modulus of the ceramic coating, t is the thickness of the plate, and υ is Poisson's ratio. In the case of solid Al_2O_3, Adkeland gives a value of 0.26 for Poisson's ratio and a value of 379,300 MPa for the elastic modulus [9]. The bending moment at the center of the plate is M_c, defined as follows:

$$M_c = \frac{qa^4(1+\upsilon)}{16} \tag{31}$$

The radial moment at the fixed edge of the plate is M_{ra}, reactive, and defined as follows:

$$M_{ra} = -\frac{qa^2}{8} \tag{32}$$

The stress on the concave surface of the deflected circular plate is compressive, and the stress on the convex surface of the deflected circular plate is tensile. The tensile stress is calculated from M_c with the following formula:

$$\sigma = \frac{6M_c}{t^2} \tag{33}$$

Assuming maximum normal stress theory for a failure criterion, failure is assumed when the stress calculated from the bending moment exceeds the fracture strength of the ceramic.

Fracture of the Protective Ceramic Coating

Growth of interfacial oxide will slowly strain the ceramic coating. The strain in the coating will induce stress. Assuming maximum normal stress theory for the failure criterion, the coating will fail at the point where the maximum stress in the ceramic coating exceeds the fracture stress. It is important to keep in mind that this failure criterion indicates fracture or a crack in the coating but does not imply that the coating has been completely removed from the substrate. The coating often appears to impart some level of continued protection in long-term corrosion tests. An order-of-magnitude estimate for fracture stresses in ceramics is used in this work. In the case of non-porous solids, the values in Table II [10] are believed to be representative of the properties of non-porous materials.

Table II. Representative Mechanical Properties of Ceramic Coatings

Ceramic	Elastic Modulus (E)	Elastic Modulus (E)	Fracture Strength (σ^*)	Fracture Strength (σ^*)
	MPa	Mpsi	MPa	Kpsi (or ksi)
Al_2O_3	365,000	53	172	25
ZrO_2	144,900	21	55	8

Others have studied environmental effects on stress corrosion cracking of thermally sprayed ceramic coatings on stainless steel and titanium substrates. Specific reference is made to studies of the environmental fracture of plasma-sprayed Al_2O_3 on metallic implants during exposures to physiological media [11]. This data is shown in Table III.

Table III. Mechanical Properties of Ceramic Coatings

Ceramic	Substrate	Environment	Fracture Strength (σ^*)	Fracture Strength (σ^*)
			MPa	Kpsi (or ksi)
Al_2O_3	Stainless Steel	Air, 26°C, 46% RH	17.8 ± 1.9	2.590 ± 0.273
Al_2O_3	Stainless Steel	Water, 25°C, Deionized	16.7 ± 1.6	2.480 ± 0.320
Al_2O_3	Titanium	Air, 26°C, 46% RH	17.1 ± 2.2	2.430 ± 0.230
Al_2O_3	Titanium	Water, 25°C, Deionized	19.1 ± 2.8	2.770 ± 0.260

Note: numbers following ± represents one standard deviation.

For the purposes of this analysis a lower limit for the likely fracture strength is selected from the lowest environmentally-sensitive fracture stress given in Table III (16.7 MPa). The data in Table II might be reasonably used as a high limit for fracture strength under optimal conditions. Unfortunately, these assignments are somewhat arbitrary approximations. A summary plot indicating the stress level for membrane stress, blister failure, and possible coating strength levels is shown in Figure 5. In this particular plot the growth of the oxide is taken to be linearly dependent on time (not parabolic growth kinetics) to keep the approximations more conservative. This figure shows that with a rather conservative assumed strength for the ceramic coating materials and a conservative assumption of Fe_3O_4 formed as the corrosion product a performance lifetime of approximately 500 years of protection against corrosion is predicted.

Experimental

Substrates of plain carbon steel (AISI 1020/UNS G10200) were coated with thermal spray techniques to produce ceramic coatings of various oxide ceramics. Oxide ceramics are selected with a preference for covalent compounds in their fully oxidized state. Alumina, Spinel ($MgAl_2O_4$), and Alumina/Titania (Al_2O_3/TiO_2) are some compositions that have been sprayed onto these substrates.

Table IV provides a summary of coatings presented in this work that were evaluated for corrosion resistance. In these experiments, 25.4 mm (1 inch) diameter steel cylindrical substrates approximately 150 mm (6 inches) long were coated by thermal spray processes. Some were exposed to the corrosion environment for nearly 6 year (5 years and 9 months). The solutions for the tanks were prepared at ten times the concentration of typical ambient groundwater and were not de-aerated. The approximate composition of some species in the solution is shown in the Table V.

Table IV. Performance of Thermal Spray Ceramic Coatings in Simulated Ten Times Concentrated Groundwater

Ceramic Type	Thermal Spray Process	Porosity (volume %)	Coating Electrical Impedance	Corrosion Conditions	General Corrosion Observation	Corrosion at Intentional Notch
Al_2O_3	Plasma Spray	~ 20%	10 Ω at 10 Hz	1st - 90°C, 6 months 2nd - 90°C, ~6 years	1st – 6 Months: Coating Blisters 2nd – ~6 years: Coating Blisters	1st – 6 months: Coating spalls at notch 2nd – ~6 years: Not Available
Al_2O_3/ TiO_2	HVOF	< 2%	100 MΩ at 10 Hz	90°C, 6 months	6 Months: None	6 months: No detectable corrosion at interface
Al_2O_3/ TiO_2 Ni bond coat	Detonation Gun	< 2%		90°C, ~6 years	~6 years: Negligible	~6 years: Small amount of corrosion at interface – attributed mostly to galvanic action

Table V. Concentration of Selected Ions (ppm) in the Corrosion Tank

Na^+	Ca^+	K^+	SO_4^{-2}	Cl^-	NO_3^-	HCO_3^-
460	30	39	180	74	64	700

For these experiments the tank was heated to 90°C and maintained with circulation. The specimens were positioned vertically so that half of the sample was above the water line. In some specimens, a notch was cut with a diamond saw along the length of the sample to penetrate through the ceramic coating into the carbon steel. The width of the notch was approximately 280 μm wide. The intent of the slot was to allow corrosion of the substrate below the ceramic coating and to examine the effects of the corrosion product upon the integrity of the thermal spray coating. The slot in this case simulates a large flaw or damage to the coating. Cross sections of the thermal spray coated specimens were made by polishing sections through the samples. In some cases etching was used to

help distinguish corrosion products from the metal substrate. The microstructures shown in this work are from the immersed portion of the specimens.

Electrical impedance measurements were made on sections of the ceramic coated thermal spray specimens. These measurements were made in the same solution described above without any prior exposure to the aqueous solution. Measurements were recorded between 10 Hz and 10 kHz.

Experimental Results and Discussion

The alumina plasma sprayed coating shown in the scanning electron micrograph in Figure 6 had a high amount of porosity approaching 20% by volume. While this is certainly not the lowest porosity that can be obtained for an alumina coating by plasma spray processes, it serves to illustrate the effect of a relatively porous coating. The obvious interconnection of the porosity seen in the planar cross-section image leads to high permeability for the aqueous solution, which provides for relatively rapid oxygen transport to the metal substrate. It should also be noted that the porosity in thermal spray coatings has a lamellar structure aligned perpendicular to the particle spray direction, which clearly can affect the diffusion though the coating. Since the lamellar shape of the porosity is clearly observable, it is likely that the three dimensional shape of the porosity in the plasma sprayed alumina coating is extensive and probably amply interconnected. In the plasma sprayed alumina microstructure shown in Figure 6 the porosity is associated with incomplete fusing or adhesion of overlaying particle splats [12]. Impedance measurements at low frequency, which we associate with the diffusive process for transport of oxygen through the thermal spray coating, show low values of impedance. The low electrical impedance implies easy transport of the oxygen through the porosity in the plasma sprayed coating. As described earlier in the analytical analysis, this can lead to rapid growth of corrosion product at the ceramic/metal interface.

In contrast, the cross-section of the HVOF sample shown in Figure 6 shows isolated porosity in the planar cross-section. In this case the overall porosity is much less, around 2% by volume. Obviously, it is possible that some connective channels may exist but they are not easily revealed in the cross-section suggesting that the capillary interconnections within the microstructure are less frequent and quite possibly rather tortuous. In the HVOF thermal spray sample, the low frequency impedance measurement shows a relatively high resistance compared to the plasma sprayed alumina ceramic coating. In fact the impedance at low frequencies is seven orders of magnitude greater in the HVOF sample. We conclude that this indicates the high resistance to diffusion of oxygen through the ceramic coating in the HVOF thermal spray coating. With regards to the processing, the high impedance at low frequency implies superior coating performance is obtained with the higher velocity thermal spray process. The lower porosity in the HVOF coating and a microstructure with reduced capillary size and/or more tortuous path provides a more resistive path for oxygen diffusion, which reduces the corrosion on the steel substrate.

The corrosion products from corrosion of the metal substrate for the plasma sprayed alumina and the HVOF alumina/titania are observed in optical micrographs in Figure 7. These micrographs show the specimens after 6 months exposure in the 90°C concentrated well water solution. In the plasma sprayed alumina sufficient amounts of corrosion product have formed at the interface between the coating and the plain carbon steel substrate such that the alumina coating begins to lift off particularly near the intentional flaw (notch) in the coating. The intentional notch was cut through the ceramic coating prior to placement of the sample in the tank. In contrast no detectable corrosion product is observed at the metal ceramic interface near a similar intentional notch in the HVOF sample. The low permeability of the HVOF coating combined with a likely improvement in bond strength associated with the lower porosity at the interface lead to no detectable corrosion product in these micrographs.

Macroscopic images of the plasma sprayed alumina specimens are shown in Figure 8 after nearly 6 years of exposure at 90°C in the salt solution described above. It can be seen that the plasma sprayed ceramic coating has blistered locally and corrosion product can be observed on top of the blisters. The steel corrosion products in some instances appear to have migrated through and remained in the pores in the plasma sprayed alumina coating. Interestingly, it does appear that with many of the blistered regions the coating remains attached to the steel substrate probably due to bonding between the corrosion product and the ceramic. For comparison a carbon steel sample exposed to the same environment (with no coating protection) is shown after less than 3 years exposure. An inset in Figure 8 shows a cross-section through several blisters of different sizes on the immersed end of the plasma sprayed alumina coating. Figure 9 is an optical micrograph showing a cross-section through a blister where the coating has been considerably disturbed and partially removed. Energy dispersive X-ray analysis of the same section of coating indicated that the coating contained substantial amounts of iron consistent with the presence of corrosion product in the pores within the ceramic coating. A portion of the coating has been dislodged from the surface in this micrograph. However, a thin layer of alumina coating has remained attached to the steel and slowed the corrosion over part of the region where the blister formed. In contrast a Detonation Gun alumina/titania coating in the Figure 8 shows no observable outward corrosion damage.

Cross-section micrographs of the Detonation Gun coating of an alumina/titania mixture are shown in Figure 10. This sample had a slot cut through the ceramic coating as well as the nickel bond coat applied to the steel before the Detonation Gun coating was applied. The microstructure around the notch in the Detonation Gun coating reveals corrosion on the interior surfaces of the notch. The nickel bond coat provides improved resistance to corrosion compared to steel, but the corrosion of the steel underneath the coating near the intentional notch has not dislodged the ceramic coating. There is some preferential corrosion at the interface between the nickel bond coat and the steel substrate. We attribute the extra corrosion in this region to galvanic coupling between the nickel and steel. In this case the nickel is more noble than the carbon steel substrate. It can be observed that the interface between the nickel and ceramic coating remains intact and the corrosion has not caused the overlying ceramic coating to spall off after a period of nearly 6 years immersed in aqueous solution at 90°C. The micrograph in

Figure 10 (b) shows a region of the coating interface far away from the notch. The gray phase appears to be a corrosion product-like phase. This was the largest amount of anything that could be interpreted as a corrosion phase observed anywhere away from the notch. It is not known if this phase was present on the steel prior to when the coating was applied. It appears that there is very little porosity in the coating. The Detonation Gun coatings are expected to have densities equivalent to or even denser than HVOF coatings.

It is interesting to note that the failure mode exhibited by the rather porous plasma sprayed alumina coatings (see Figure 8) appears to be the blister failure mode which is consistent with the theory-based prediction (for the typical coating properties mentioned above). The results of the analytical calculations indicate higher stress in the blister failure mode as shown in Figure 5. Figure 7 indicates a coating displacement of up to 350 μm has occurred in 6 months time in the plasma sprayed alumina coating. Considering just the simple calculation of strain in the Membrane Stress Failure Criterion, a strain in this coating can be calculated. For the 25.4 mm diameter steel substrate this amount of corrosion product corresponds to 2.8% strain, which significantly exceeds the 0.0047% lower limit failure strain (equation 26). This result indicates the failure of highly porous coatings while the results from the HVOF and Detonation Gun coatings indicate that long lifetimes may be possible with low porosity in the coatings. Additional experiments would be useful to provide greater experimental confidence in the analytical calculations. If a higher strength for the coatings is assumed, a longer life of about 6000 years is predicted in the calculation results in Figure 5. It is quite possible that this length of time would protect a waste package against corrosion during the highest temperature portion of the waste package lifetime and continue to provide protection as the radioactive decay eventually leads to lower temperatures in the waste container.

Summary

A set of analytical calculations based on fundamental corrosion theory and mechanical failure criteria for the performance of the ceramic coatings in aqueous corrosion environments is postulated to guide predictions based on assumed microstructural and physical properties for thermal spray coatings. The calculations suggest that with the proper microstructure and physical properties a ceramic thermal spray coating will provide significant corrosion protection lifetimes. It was observed that the blister failure mode caused the first failures in a highly porous ceramic coating, which was consistent with the coating stress calculations. It is evident from the experimental results that ceramic coatings with sufficiently low porosity can provide a sufficient barrier against aqueous corrosion in ten times concentrated groundwater solutions at 90°C. In particular a Detonation Gun coating tested under these conditions for nearly 6 years demonstrated resistance to corrosion damage of the underlying steel substrate even with an intentional defect (a 280 μm thick slot) cut through the coating to the steel substrate.

Acknowledgements
The authors acknowledge the assistance of Tom Shell, Dan McCright, John Estill, David Fix, S. Daniel Day, Lana Wong, Raul Rebak, Bob Vallier, and Jackson Go for assistance with specimens, analysis, and useful discussions of results.

List of Figure Captions

Figure 1. This is an illustration of parameters associated with diffusion of oxygen through inorganic coating. Subscript, *I*, is associated with the ceramic coating and subscript, *0*, is associated with the iron oxide corrosion product.

Figure 2. This is an illustration of idealized porosity used to model the pore structure in the ceramic thermal spray coatings, which is called the Cylinder-Sphere Chain (CSC) porosity model.

Figure 3. This figure illustrates the model of stress in an expanded cylinder. As in Figure 1, subscript, *I*, is associated with the ceramic coating and subscript, *0*, is associated with the iron oxide corrosion product.

Figure 4. This is an illustration of the blister model for failure of the ceramic coating due to localized growth of oxide underneath the ceramic coating. The load applied to the coating due to the oxide growth is q, and the radius of the blister is a. M_c is the critical bending moment that produces tensile strain leading to failure in the blister.

Figure 5. This plot shows stress predicted in the coating due to blister and membrane stress failure mechanisms. A range of possible strengths for the ceramic coatings (as described in the text) is indicated. This strength range provides a range of possible lifetimes based on the analytical calculations and the assumptions used in the theoretical

development. For the calculation of membrane stress the radius of the substrate was 1 meter. As a conservative measure in this analysis, the oxide grows linearly with time rather than the typical parabolic growth rate.

Figure 6. Microstructure and impedance resistance measurements for HVOF coated alumina/titania and plasma sprayed alumina. The large arrow indicates the thermal spray direction.

Figure 7. Microstructures of long-term test specimens after 6 months in ten times concentrated groundwater solution at 90°C. HVOF thermal spray coating (top) and plasma spray coating (bottom) are shown. The machine cuts in the images on the left were made before the samples were exposed to the aqueous environment.

Figure 8. This figure shows macroscopic images of (a) ceramic coated steel specimens in racks as situated in corrosion tanks, (b) low carbon steel exposed to same conditions for less than 3 years, (c) close up of plasma sprayed alumina sample on left and Detonation Gun alumina/titania sample on right after nearly 6 years in 90°C salt solution. The waterline is approximately half way up the sample. The blistering in the plasma sprayed alumina coating is attributed to the high porosity in the coating, which allows for rapid corrosion under the ceramic coating. The discoloration on the Detonation Gun coating was from salts in the water solution, which have adsorbed onto the surface. Underneath the surface contaminates, the coating appears to have the original color. Epoxy-mounted metallographic cross-section samples (insets) were taken from below the water line. The

arrows indicate the approximate cross-section location. The ceramic coating is a black layer of uniform thickness in the Detonation Gun coating (top). An intentional notch is located at the top of the metallographic image for the Detonation Gun Coating. The cross-section passes through blisters in the Plasma Sprayed alumina coating (bottom).

Figure 9. Micrograph of the cross-section of the plasma sprayed alumina coating on a carbon steel substrate. Fracture of the coating at a blister and the formation of corrosion product under the coating are shown in the micrograph. In particular corrosion at the edges of the blister can be seen.

Figure 10. This micrograph shows the Detonation Gun coating of Alumina/Titania mixture on top of a nickel bond coat. The substrate is plain carbon steel. (a) The slot was cut in the coating prior to placing it in a 90°C corrosion tank. This micrograph is from a slot that was immersed in the aqueous solution for nearly 6 years. (b) This micrograph is from a region far away from the slot. The gray phase is believed to be an iron oxide and was the largest "corrosion-like" phase observed at the interface away from the slot. It is not certain whether the oxide was already present on the steel prior to the application of the coating. The large black lamellar particles in the coating are believed to be solid; no large pores are easily observed.

Figures

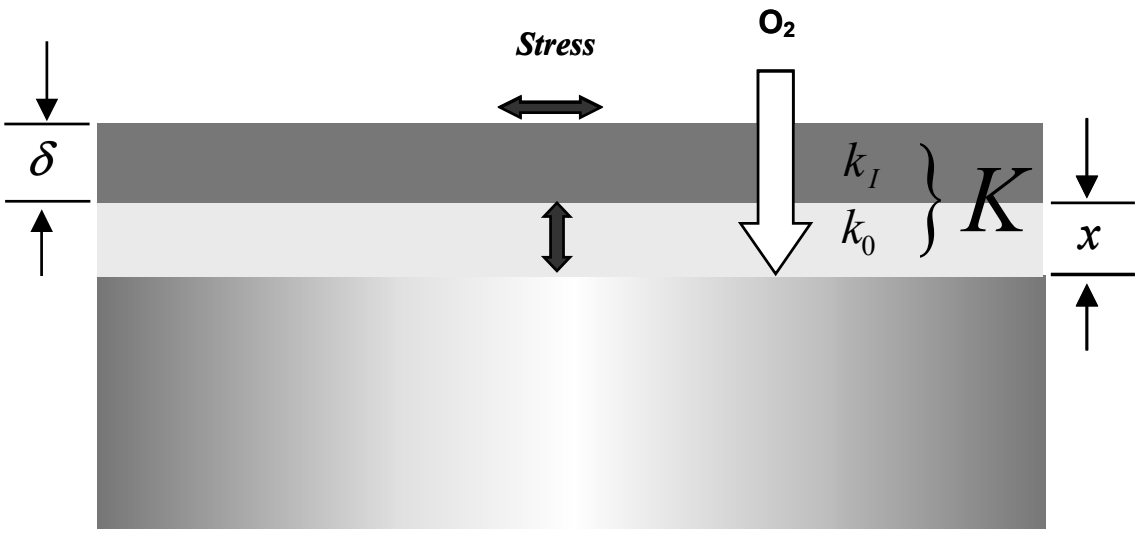

Figure 1. This is an illustration of parameters associated with diffusion of oxygen through inorganic coating. Subscript, *I*, is associated with the ceramic coating and subscript, *0*, is associated with the iron oxide corrosion product.

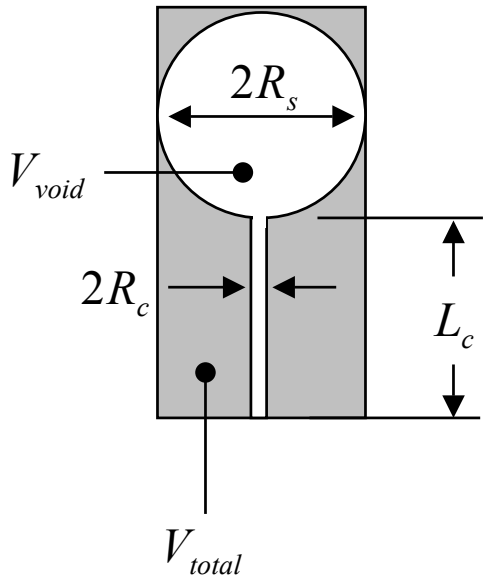

$$\varepsilon = \frac{2R_c}{2R_s}$$

$$\lambda = \frac{L_c}{2R_s}$$

Figure 2. This is an illustration of idealized porosity used to model the pore structure in the ceramic thermal spray coatings, which is called the Cylinder-Sphere Chain (CSC) porosity model.

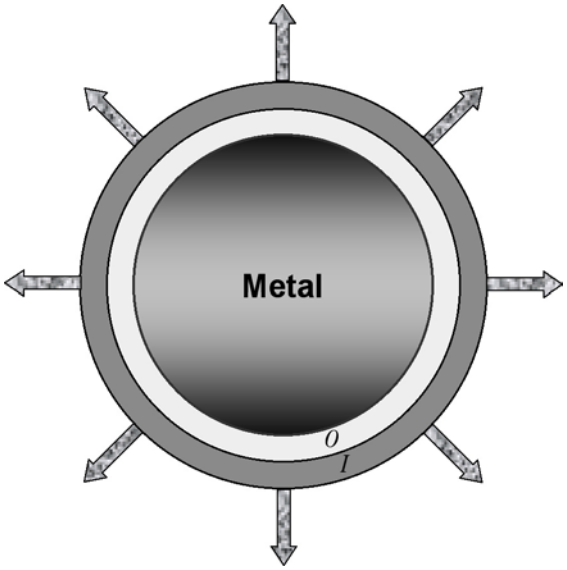

Figure 3. This figure illustrates the model of stress in an expanded cylinder. As in Figure 1, subscript, *I*, is associated with the ceramic coating and subscript, *0*, is associated with the iron oxide corrosion product.

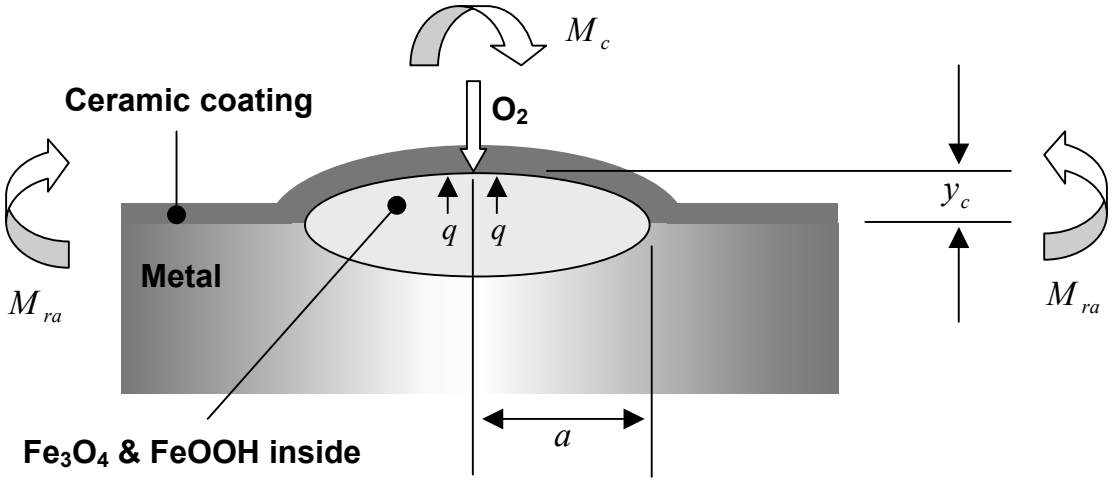

Figure 4. This is an illustration of the blister model for failure of the ceramic coating due to localized growth of oxide underneath the ceramic coating. The load applied to the coating due to the oxide growth is q, and the radius of the blister is a. M_c is the critical bending moment that produces tensile strain leading to failure in the blister.

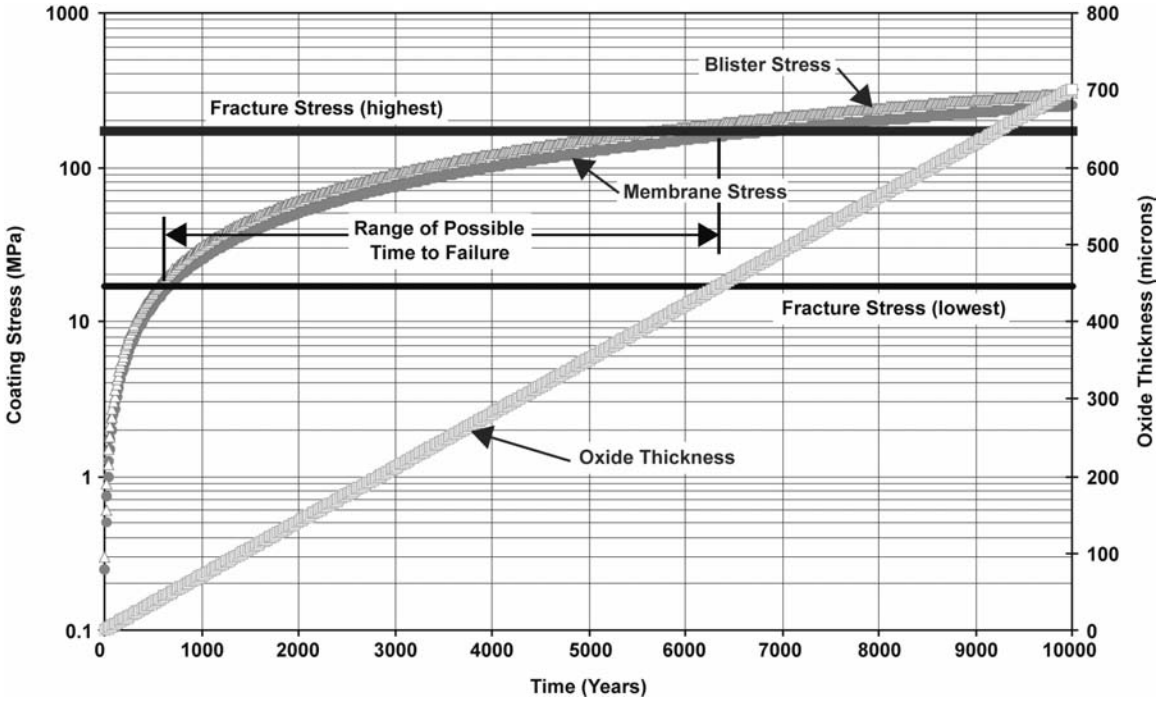

Figure 5. This plot shows stress predicted in the coating due to blister and membrane stress failure mechanisms. A range of possible strengths for the ceramic coatings (as described in the text) is indicated. This strength range provides a range of possible lifetimes based on the analytical calculations and the assumptions used in the theoretical development. For the calculation of membrane stress the radius of the substrate was 1 meter. As a conservative measure in this analysis, the oxide grows linearly with time rather than the typical parabolic growth rate.

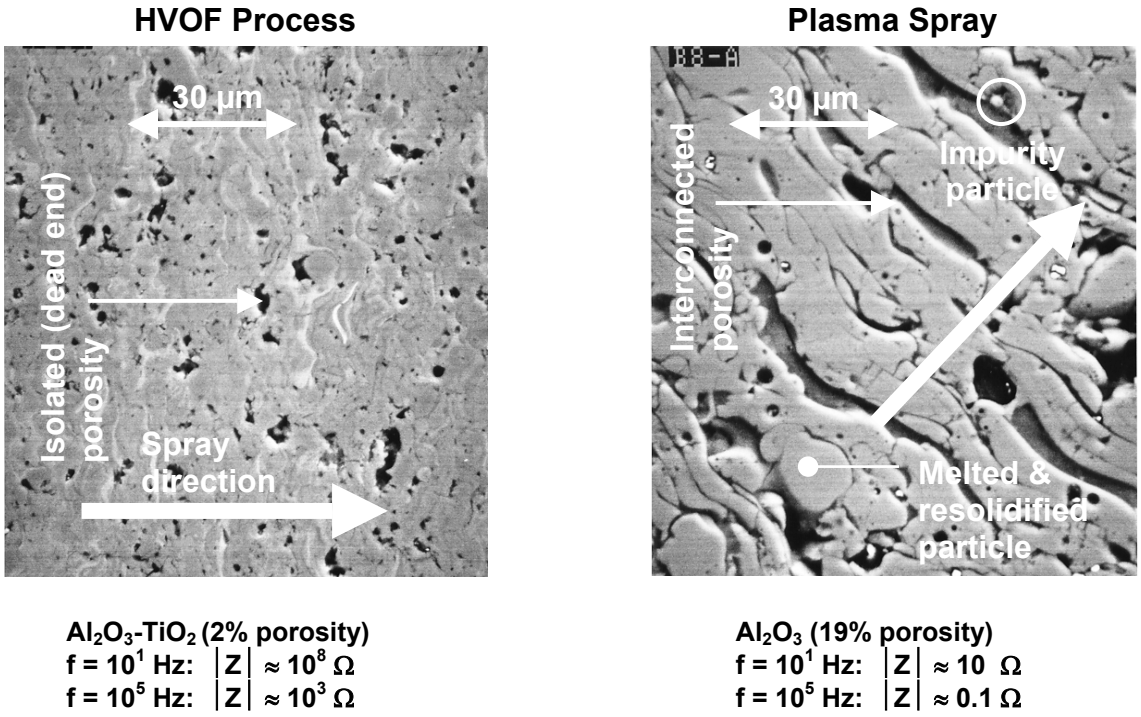

Figure 6. Microstructure and impedance resistance measurements for HVOF coated alumina/titania and plasma sprayed alumina. The large arrow indicates the thermal spray direction.

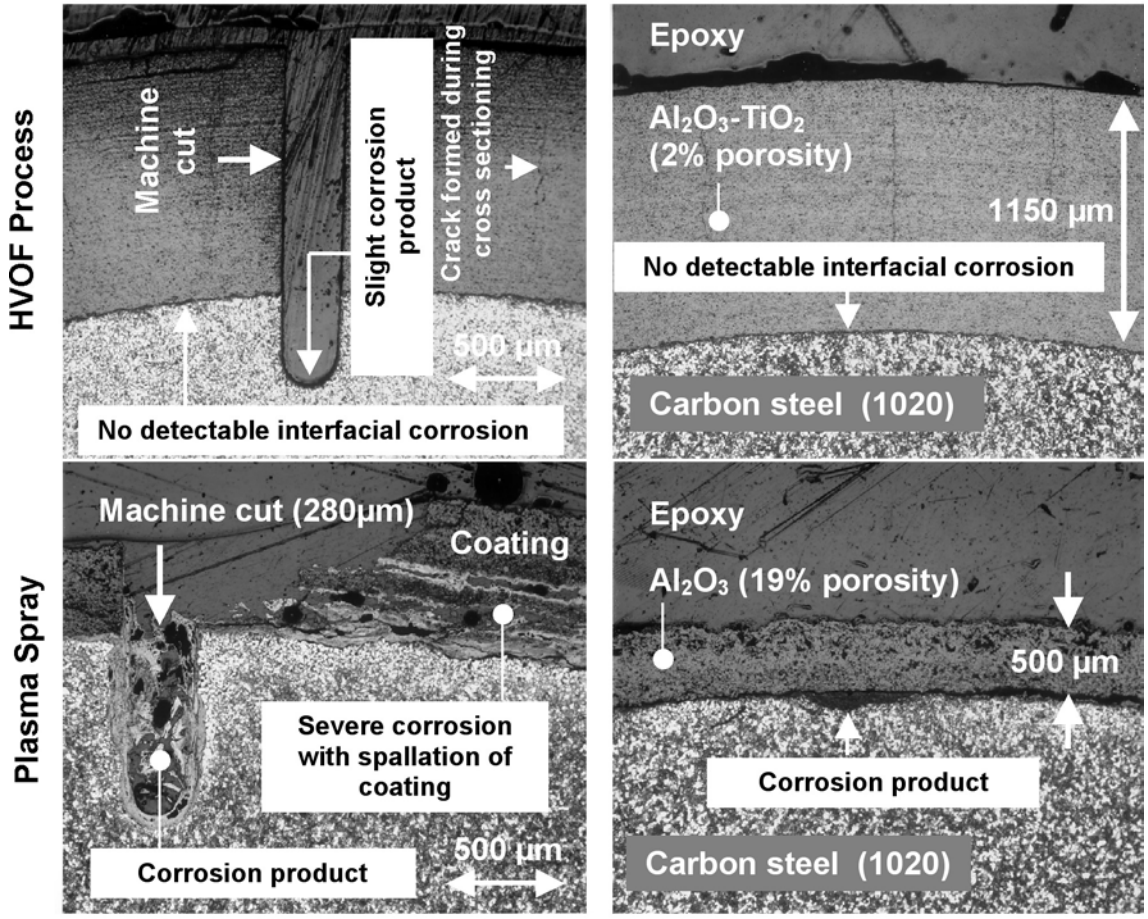

Figure 7. Microstructures of long-term test specimens after 6 months in ten times concentrated groundwater solution at 90°C. HVOF thermal spray coating (top) and plasma spray coating (bottom) are shown. The machine cuts in the images on the left were made before the samples were exposed to the aqueous environment.

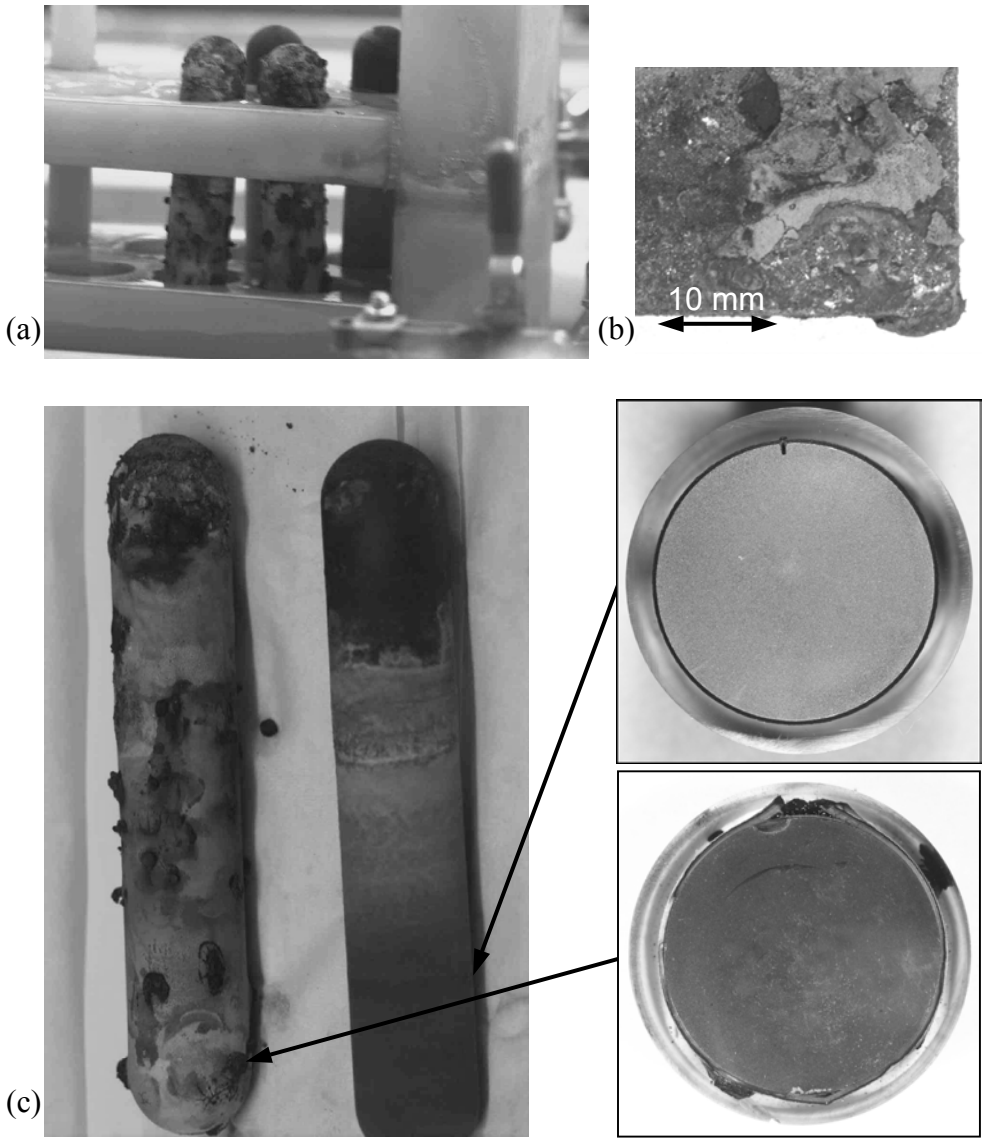

Figure 8. This figure shows macroscopic images of (a) ceramic coated steel specimens in racks as situated in corrosion tanks, (b) low carbon steel exposed to same conditions for less than 3 years, (c) close up of plasma sprayed alumina sample on left and Detonation Gun alumina/titania sample on right after nearly 6 years in 90°C salt solution. The waterline is approximately half way up the sample. The blistering in the plasma sprayed alumina coating is attributed to the high porosity in the coating, which allows for rapid corrosion under the ceramic coating. The discoloration on the Detonation Gun coating was from salts in the water solution, which have adsorbed onto the surface. Underneath the surface contaminates, the coating appears to have the original color. Epoxy-mounted metallographic cross-section samples (insets) were taken from below the water line. The arrows indicate the approximate cross-section location. The ceramic coating is a black layer of uniform thickness in the Detonation Gun coating (top). An intentional notch is located at the top of the metallographic image for the Detonation Gun Coating. The cross-section passes through blisters in the Plasma Sprayed alumina coating (bottom).

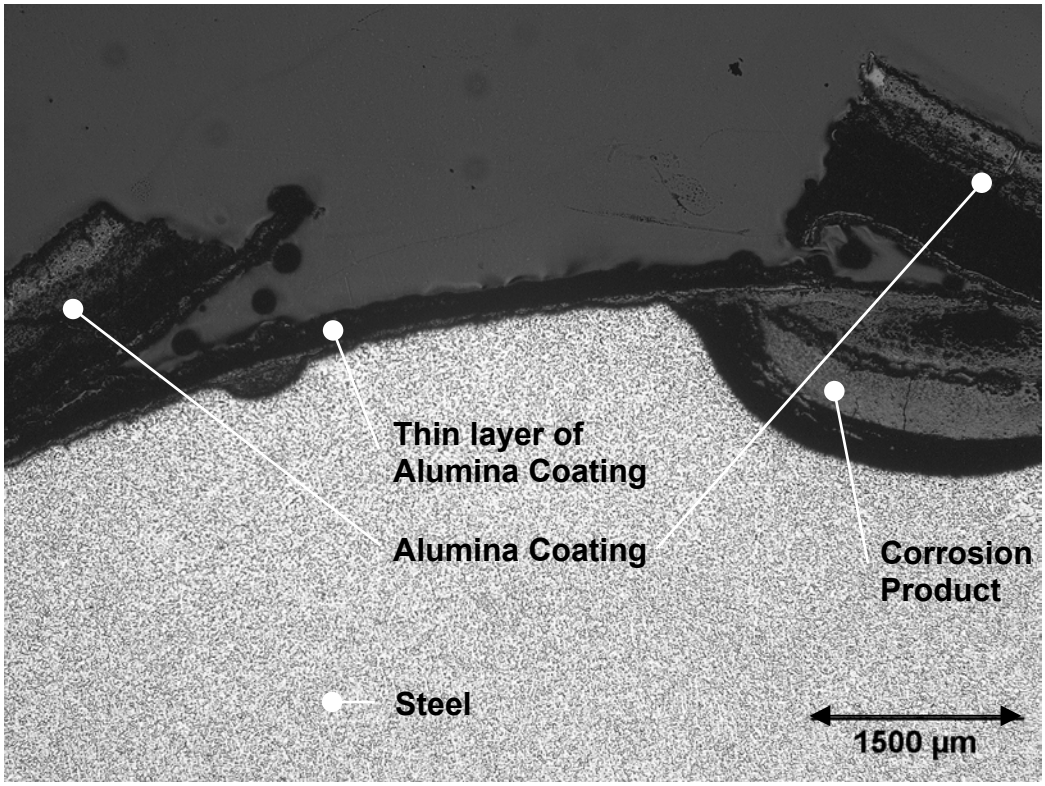

Figure 9. Micrograph of the cross-section of the plasma sprayed alumina coating on a carbon steel substrate. Fracture of the coating at a blister and the formation of corrosion product under the coating are shown in the micrograph. In particular corrosion at the edges of the blister can be seen.

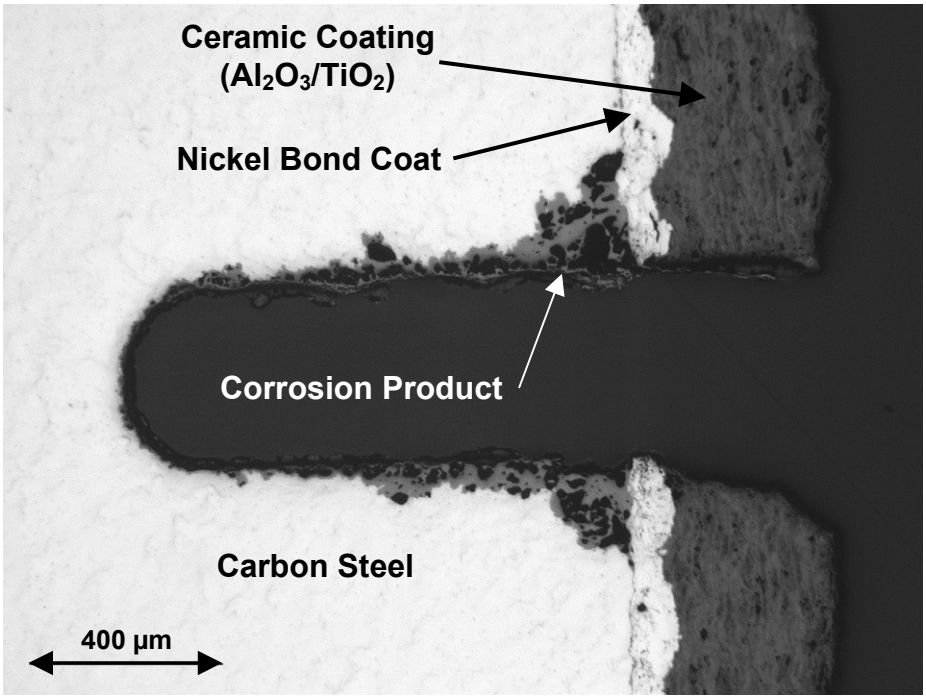

(a)

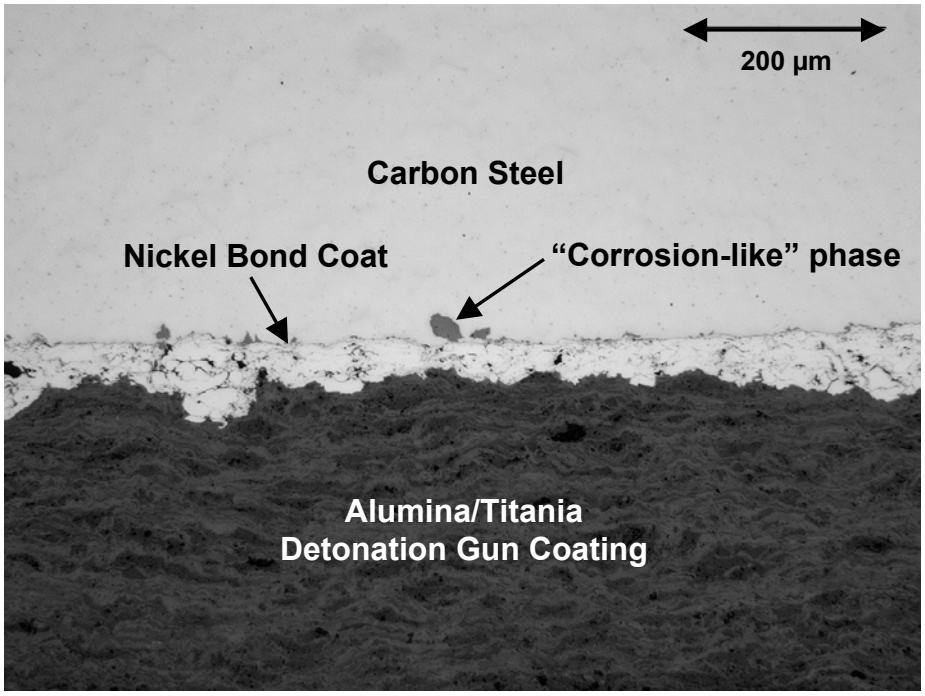

(b)

Figure 10. This micrograph shows the Detonation Gun coating of Alumina/Titania mixture on top of a nickel bond coat. The substrate is plain carbon steel. (a) The slot was cut in the coating prior to placing it in a 90°C corrosion tank. This micrograph is from a slot that was immersed in the aqueous solution for nearly 6 years. (b) This micrograph is from a region far away from the slot. The gray phase is believed to be an iron oxide and was the largest "corrosion-like" phase observed at the interface away from the slot. It is not certain whether the oxide was already present on the steel prior to the application of the coating. The large black lamellar particles in the coating are believed to be solid; no large pores are easily observed.

7 References

[1] R. D. McCright: MRS Bull., 1994, December, pp. 39-42.

[2] R. C. Tucker, Jr.: Advanced Thermal Spray Deposition Techniques in Handbook of Deposition Technologies for Films and Coatings / Science, Technology and Applications, 2nd Edition, Edited by Rointan F. Bunshah, Noyes Publications, Park Ridge, NJ, 1994, p. 647.

[3] R.C. Tucker, Jr.: Advanced Thermal Spray Deposition Techniques in Handbook of Deposition Technologies for Films and Coatings / Science, Technology and Applications, 2nd Edition, Edited by Rointan F. Bunshah, Noyes Publications, Park Ridge, NJ, 1994, pp. 617-629.

[4] J. C. Farmer and K. R. Wilfinger: Internal Report, UCRL-ID-131899 Rev. 1, Lawrence Livermore National Laboratory, Livermore, CA, September 1998.

[5] H.H. Uhlig, R. W. Revie: Corrosion and Corrosion Control, 3rd Edition, Wiley Interscience, New York, NY, 1985, p. 108; Corrosion in the Petrochemical Industry, L. Garverick, Editor, ASM International, 1994, p. 450.

[6] D. R. Kester: Dissolved Gases Other Than CO_2, Chemical Oceanography, Vol. 1, 2nd Ed, J. P. Riley, G. Skirrow, Editors, Academic Press, 1973, p. 498; Metals Handbook, Vol. 13, ASM, CD ROM Version, 1998.

[7] T.K. Sherwood, R.L. Pigford and C.R. Wilke: Mass Transfer, McGraw-Hill, San Francisco, CA, 1975, pp. 25-26.

[8] W. C. Young: Roark's Formulas for Stress and Strain, 6th Ed., McGraw-Hill, San Francisco, CA, 1989, p. 429.

[9] D. R. Adkeland, The Science and Engineering of Materials, 3rd Ed., PWS Publishing, Boston, MA, 1994, p. 141.

[10] P.A. Thornton, V. J. Colangelo, Fundamentals of Engineering Materials, Prentice Hall, Englewood Cliffs, NJ, 07632, 1985.

[11] M. K. Ferber and S. D. Brown: Adhesive/Cohesive Fracture Characteristics of Plasma-Sprayed Alumina Coatings Applied To 316L Stainless Steel and Ti-6Al-4V ELI Alloy Substrates in Various Physiological Media, in Fracture Mechanics of Ceramics, Vol. 6, Measurements, Transformations, and High-Temperature Fracture, R. C. Bradt, A. G. Evans, D. P. H. Hasselman, F. F. Lange, Plenum Press, New York, NY, 1983, pp. 523-544.

[12] A. Kulkarni, A. Vaidya, A. Goland, S. Sampath, and H. Herman: Matrls. Eng. A, 2003, vol. A359, pp. 100-111.

[13] J. D. Bernal, "The Structure of Liquids," Proc. Roy. Soc. (London) A **280**, 1964, p. 299.

[14] F. A. L. Dullen, *Porous Media: Fluid Transport and Pore Structure,* Second Edition, Academic Press, 1992.

Appendix A

The porosity models used are relatively basic. They are intended to elucidate the relative importance of the main features of the ceramic microstructure, to show the quantitative forms that result, and to provide very approximate estimates of the absolute value of the reduction in the corrosion rate that can be expected. This approach is warranted by the wide variation of the porosity with coating method and process parameters, as evidenced by Figure 6, and by the lack of any comprehensive characterization of the actual porosity structures encountered. Little would be gained by extensive elaborations on the basic model. It is nevertheless worthwhile taking the basic CSC model a step or two further.

First we review the analysis of the diffusive transport through a single cylinder-and-sphere link, depicted in Figure 2. The total molar transport through the link is denoted q and is fixed. The concentration drops through the sphere, ΔC_s, and through the cylinder, ΔC_c, are then calculated. Then the transport q^* through an "equivalent" cylinder having the same volume and total length as the cylinder-sphere link, for the same concentration drop, is calculated. The ratio gives the comparison factor $f(\varepsilon,\lambda) = q/q^*$. The calculation of ΔC_c is elementary. The calculation of ΔC_s consists of solving Laplace's equation (steady diffusion) for a sphere of radius R_s having an inward flow q over a small spherical cap of radius R_c at one pole and exiting a similar one at the other. (Three boundary conditions were investigated: constant radial flux, constant axial flux, and constant concentration. The first of these is the simplest, and the differences in the result the other boundary conditions were insignificant. In each case, a standard series solution in spherical harmonics was used.) The resistance to transport is heavily dominated by the cylinders.

In the basic CSC straight-chain model of n links per chain, the total length is $n(2R_s + L_c)$ and the total concentration drop is $n(\Delta C_s + \Delta C_c)$. An excessively accurate approximation of the results was obtained, which in turn was approximated by equation 12, which gives ample accuracy when $\varepsilon < 0.2$ and $\lambda > 0.2$ (cf. equations 16 and 17).

An improved random-network porosity model, mentioned in the text, builds on the foregoing. The porosity is again imagined to consist of large holes and slender channels. The holes are all spheres of the same radius, and the channels are all cylinders of the same diameter and length. The cylinders are oriented randomly and connect to two spheres. Each sphere is connected to four cylinders. The net result of averaging over such a structure is merely that the factor of 3/2 in the approximate $f(\varepsilon,\lambda)$ given by equation 12 disappears. This model adds the effects of coordination and tortuosity to the effect of varicosity included in the basic CSC model. The overall resistance to diffusive transport continues to be dominated by transport in the slender channels (when the total volumetric porosity is the same).

Such a structure is not an actual microstructure but is not a bad approximation to the physically-realizable tetrahedral random networks that are good approximations to the structures of certain glasses, notably amorphous silicon. Drawing this comparison is specious, however, for the microstructures arising from the thermal spray process are probably very different. A better conceptual model is a "random close packing" (RCP)

of spheres (also known by other names). A modern systematic study was initiated by Bernal [13] as a model of simple liquids and has since been found to be widely useful. Dullen [14] has used them to model transport through porous media. In a RCP, 73% of the holes have four channels emanating from them, and ~20% have five. The remaining holes are quite large and probably are not relevant in the present context. Aside from the range of coordination, the channel angles and lengths vary more than in the tetrahedral random networks. Incorporating the known statistics of the RCP models is the sort of refinement to be eschewed in the present context.

A potentially more important improvement, which has not been undertaken by the authors, is to recognize the anisotropy of the thermal spray coatings. The particles deform considerably upon impact (they are often termed "splats"). This seems rather severe for our plasma-sprayed coatings but possibly less so for the HVOF process (see Figure 6). Various models might be conceived, such as disk-like holes located randomly but oriented parallel to the metal substrate, connected by non-collinear cylindrical channels.

Appendix B

Prior to integration, the overall mass transfer coefficient must be rewritten in terms of oxide thickness:

$$\int_{x_0}^{x}\left[\frac{x}{\theta_0 D_0}+\frac{\delta}{f(\varepsilon,\lambda)\theta_I D_I}\right]dx=\int_{t_0}^{t}\frac{1}{2}\frac{w_0}{\rho_0}C\,dt \tag{B1}$$

Integration shows that the oxide thickness and time are related by a simple quadratic equation:

$$\left[\frac{1}{2\theta_0 D_0}\right]x^2+\left[\frac{\delta}{f(\varepsilon,\lambda)\theta_I D_I}\right]x-\frac{1}{2}\frac{w_0}{\rho_0}C\,t=0 \tag{B2}$$

Solution of this simple quadratic equation yields the following relationship between oxide thickness, time and ceramic coating properties:

$$x=\left[\left\{\frac{\delta}{f(\varepsilon,\lambda)}\frac{\theta_0 D_0}{\theta_I D_I}\right\}^2+(\theta_0 D_0)\frac{w_0}{\rho_0}C\,t\right]^{1/2}-\left\{\frac{\delta}{f(\varepsilon,\lambda)}\frac{\theta_0 D_0}{\theta_I D_I}\right\} \tag{B3}$$